

CHARACTERIZATION OF THE DISTRIBUTION OF THE $\text{Ly}\alpha$ EMITTERS IN THE 53W002 FIELD AT $z = 2.4$ ¹

K. Mawatari, T. Yamada and Y. Nakamura

Astronomical Institute, Tohoku University, Aoba, Aramaki, Aoba-ku, Sendai, Miyagi, 980-8578, Japan
 mawatari@astr.tohoku.ac.jp

T. Hayashino

Research Center for Neutrino Science, Graduate School of Science, Tohoku University, Sendai 980-8578, Japan
 and

Y. Matsuda

National Astronomical Observatory of Japan, Mitaka, Tokyo 181-8588, Japan

ABSTRACT

We present the results of our wide-field narrow band imaging of the field around the radio galaxy 53W002 at $z = 2.390$ with Subaru/Suprime-Cam. A custom made filter *NB413* centered at 4140 \AA with the width of 83 \AA is used to observe the $31' \times 24'$ area around the radio galaxy. We detected 204 $\text{Ly}\alpha$ emitters (LAEs) at $z = 2.4$ with a rest frame equivalent width larger than 25 \AA to the depth of 26 AB mag (in *NB413*). The entire LAE population in the 53W002 field has an average number density and distributions of equivalent width and size that are similar to those of other fields at $z \sim 2$. We identify a significant high density region (53W002F-HDR) that spreads over $\approx 5' \times 4'$ near 53W002 where the LAE number density is nearly four times as large as the average of the entire field. Using the probability distribution function of density fluctuation, we evaluate the rareness probability of the 53W002F-HDR to be $0.9_{-0.62}^{+2.4} \%$, which corresponds to a moderately rich structure. No notable environmental dependency at the comoving scale of 10 Mpc is found for the distributions of the $\text{Ly}\alpha$ equivalent width and luminosity in the field. We also detected 4 $\text{Ly}\alpha$ blobs (LABs), one of which is newly discovered. They are all found to be located in the rims of high density regions. The biased location and unique morphologies in $\text{Ly}\alpha$ suggest that galaxy interaction play a key role in their formation.

Subject headings: cosmology: observations — galaxies: evolution — galaxies: formation — large-scale structure of universe

1. INTRODUCTION

In the local universe, a strong environmental dependence of galaxy properties is observed (e.g. Dressler 1980; Binggeli et al. 1988; Goto et al.

2003; Park et al. 2007). It is understood that external effects from their surrounding environments, namely galaxy-galaxy merger, harassment, ram-pressure stripping, and starvation may play key roles in sufficiently mature structures like clusters of galaxies in the nearby universe. At high redshift, on the other hand, the intrinsic environmental effects, such as galaxy formation bias

¹Based on the observations conducted with the Subaru Telescope which is operated by the National Astronomical Observatory of Japan.

(Benson et al. 2001; Weinberg et al. 2004) should also play an important role rather than the external effects. The high density regions at high redshift are dominated by star-forming galaxies as galaxy formation preferentially occurs in dense environments at such epochs, which is naturally expected in the hierarchical structure formation theories. Observations of high- z protoclusters are important in order to study how such intrinsic environmental effects work on the galaxies in the early universe.

So far the narrow band method has been very efficient to discover density excesses at high redshift. Many authors have searched and discovered overdense structures traced by Ly α emitters (LAEs) since the late 1990s (e.g., $z \sim 2$: Pentericci et al. 2000; Prescott et al. 2008, $z \sim 3$: Steidel et al. 2000; Hayashino et al. 2004; Yamada et al. 2012, $z \sim 4$: Venemans et al. 2002; Kuiper et al. 2011, $z \sim 5$: Shimasaku et al. 2003; Venemans et al. 2004, $z \sim 6$: Ouchi et al. 2005). LAEs are thought to be less massive, metal-poor, young and star-forming galaxies in general (Malhotra & Rhoads 2002) although it is reported recently that their properties may change along redshift (Nilsson et al. 2009; Nakajima et al. 2012). Ono et al. (2010) reported the typical physical quantities of LAEs at $z = 3 - 4$: $M_{star} = 10^8 - 10^{8.5} M_{\odot}$, $SFR = 1 - 100 M_{\odot} yr^{-1}$, ages = $10^6 - 10^9$ yr, $E(B-V) < 0.2$. Such a galaxy population at high redshift is considered to trace the large scale structure (Uchimoto et al. 2012), and at least some fraction of them should be the building-blocks that evolve to massive galaxies at the later epochs.

The distributions of Ly α emitters in the field around the radio galaxy 53W002 at $z = 2.39$ and $\alpha = 17^h 14^m 14^s.8$, $\delta = +50^{\circ} 15' 49''$ (hereafter, the 53W002 field), which is the region we study in this paper, was first investigated by Pascarelle et al. (1996a,b). They conducted deep medium-band ($\Delta\lambda = 150 \text{ \AA}$) imaging of the 53W002 field using *Hubble Space Telescope (HST)*/Wide Field and Planetary Camera 2 (WFPC2). In their relatively small survey area ($\sim 2.5' \times 2.5'$), 18 LAEs at $z \sim 2.4$ were discovered, which was claimed to be the first direct detection of so-called ‘building-blocks’ of galaxies at high redshift. Pascarelle et al. (1998) also observed three other WFPC2 fields using the same medium-band

filter and argued that the 53W002 field is a high density region. Keel et al. (1999) then surveyed the wider area around 53W002 with the 4 m Mayall telescope of Kitt Peak National Observatory. They found 14 LAEs in the area of $14' \times 14'$ and suggested that the LAEs in the 53W002 field showed density excess compared with those in the blank fields. While several authors have investigated the properties of the galaxies in this field (Windhorst et al. 1998; Waddington 1998; Yamada et al. 2001; Motohara et al. 2001a,b; Im et al. 2002; Keel et al. 2002; Smail et al. 2003), the previous observations seem to be insufficient to establish the significance of the density enhancement of the field. First, the medium-band filters used to detect Ly α emission line in the previous observations covers the relatively wide redshift range of $\Delta z = 0.12$ ($z = 2.30 - 2.42$), which may suffer from some projection effects. Second, both deep and wide observations are essential to identify the high redshift overdense region while the previous observations are not sufficient either in area (*HST* observation) or in depth (ground-based observation).

It is important not only to detect the high density regions at high redshift but also to characterize their richness in order to trace the evolution of galaxies in such dense environments or to compare the properties of the galaxies in their appropriate descendants. It is needed to introduce some objective measure to characterize such high-density overdense regions selected by LAEs to make the ancestors/descendants comparison possible.

In this paper, we present the results of our deep and wide observations using the narrow-band filter. We describe the observation and data reduction in §2, sample selection of LAEs in §3, and the results in §4. In §5, we discuss the implications of our results. Our conclusions are summarized in §6. Throughout this paper, we use AB magnitude system and adopt a cosmology with $H_0 = 70.5 \text{ km s}^{-1} \text{ Mpc}^{-1}$, $\Omega_M = 0.27$, and $\Omega_{\Lambda} = 0.73$ (Komatsu et al. 2009).

2. OBSERVATION AND REDUCTION

In 2009 May 22 - 23 (UT), we carried out imaging observations of the 53W002 field, centered at $\alpha = 17^h 14^m 15^s.2$, $\delta = +50^{\circ} 15' 49''$ (J2000) using Suprime-Cam (Miyazaki et al. 2002) equipped on the 8.2 m Subaru telescope. We used the cus-

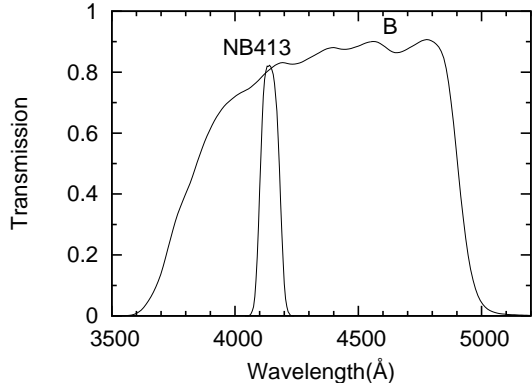


Fig. 1.— Transmission curves of the filters we used: Subaru/Suprime-Cam B -band and the custom-made $NB413$.

tom narrow-band filter $NB413$ which has the central wavelength of 4140 \AA and the width of 83 \AA ($FWHM$). The $NB413$ filter was built aiming to detect $\text{Ly}\alpha$ emission at $z = 2.37 - 2.44$. We also used the B -band filter to estimate the continuum flux. In Figure 1 we show the transmission curves of the filters used in this study. The total exposure time was 3.5 hours for the $NB413$ and 1 hour for the B band, respectively.

We used SDFRED version 2.0 (Yagi et al. 2002; Ouchi et al. 2004) for the data reduction. As the number of the exposures is small (7 shots for the $NB413$ images), we made careful cosmic ray subtraction using L.A.Cosmic (van Dokkum 2001) after the flat-fielding. We also masked the areas where bright stars affect the images. The final mosaiced images have the field of view (FoV) of $31.3' \times 23.7'$ and the available area of 707.1 arcmin^2 . This roughly corresponds to $50 \text{ Mpc} \times 40 \text{ Mpc}$ in comoving scale. The width of $NB413$ filter corresponds to 90 Mpc . Our survey comoving volume for LAEs at $z = 2.4$ is $1.75 \times 10^5 \text{ Mpc}^3$. The B band image was smoothed so that the size of the stellar images is matched to that of the $NB413$ image; $0.86''$ in $FWHM$. The flux calibration was made by using the spectroscopic standard star, PG1708+602. We used SExtractor (Bertin & Arnoult 1996) version 2.5.0 for object detection and photometry. The resultant 5σ limiting magnitude in $2''$ -diameter aperture is 25.95 mag for the $NB413$ image and 26.7 mag for the B image. The 5σ limiting magnitude of the $NB413$

image corresponds to the narrow-band luminosity (L_{NB413}) of $1.0 \times 10^{42} \text{ erg s}^{-1}$ assuming objects at $z = 2.4$.

3. SELECTION OF LAE

Object detection was made on the $NB413$ image: we adopted the criteria that more than 12 contiguous pixels above the 3σ threshold of the background fluctuation. Furthermore, we rejected the obvious false detections using one of the SExtractor parameters, FLAGS. As a result, a total of $\sim 28,000$ objects were detected in the range of $17 \text{ mag} \leq NB413 \leq 27 \text{ mag}$. In the photometry, we used the fixed diameter ($2''$) aperture for both of the $NB413$ and the B images, where each aperture was centered on the position of the object detected in the $NB413$ image. For objects fainter than 1σ limiting magnitude in the B band image, we replaced their B band magnitude with 1σ (28.45 mag).

To select the LAE candidates, we adopted the following three selection criteria. (i) $B - NB413 \geq 0.68$: the $B - NB413$ color of 0.68 corresponds to the rest-frame equivalent width (EW_0) of 25 \AA for $z = 2.4$ $\text{Ly}\alpha$ emission line. (ii) $18 \text{ mag} \leq NB413 \leq 25.95 \text{ mag}$. (iii) $B - NB413 \geq -0.2 + 4\sigma$ in the color. The last criterion is to avoid the contamination at the faint end, where the foreground or background objects distribute around $B - NB413 = -0.2$. For the 213 objects which satisfy the three criteria, we visually inspected them to reject 9 sources (e.g. saturated stars, part of extended blobs). We finally accepted the remaining 204 objects as significant emission-line objects. These 204 candidates are shown in the color-magnitude diagram of Figure 2.

One possible contaminant for $z = 2.4$ LAE is an [O II] emitter at $z = 0.10 - 0.12$. Our 5σ detection limit of the $NB413$ image corresponds to the [O II] luminosity of $L = 6.8 \times 10^{38} \text{ erg s}^{-1}$ and the surveyed comoving volume is $\sim 1,150 \text{ Mpc}^3$, which is one hundred times smaller than that for $\text{Ly}\alpha$ at $z = 2.4$. From the luminosity function and EW distribution in Sullivan et al. (2000) we expect ~ 7 [O II] emitters in our sample. While another possible contaminant is a C IV emitter at $z = 1.65 - 1.70$, a strong C IV emission line is expected only among AGN whose number density is much smaller than [O II] emitters or $\text{Ly}\alpha$ emitters. Considering the above, contamination can

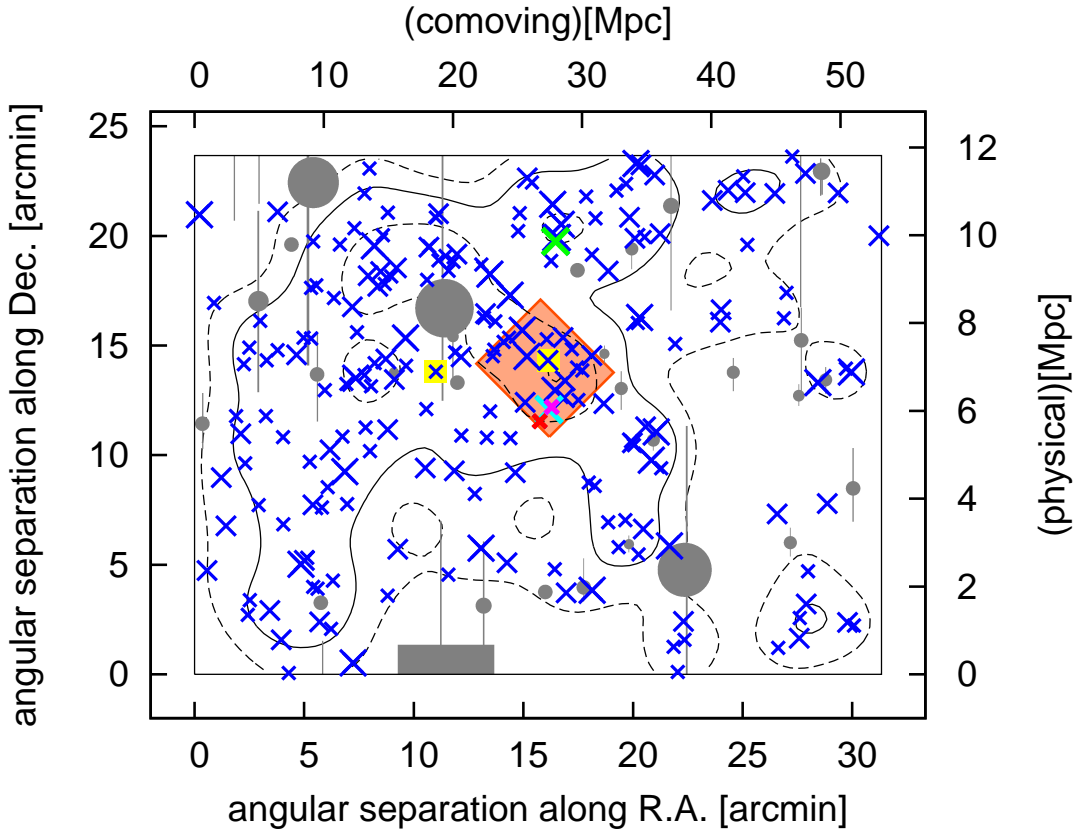


Fig. 3.— Sky distribution of the 204 LAEs in the 53W002 field (*blue crosses*), which include extended Ly α Blobs (53W002: *red cross*, No.18: *cyan cross*, No.19: *magenta cross*, and LAB4: *green cross*) and QSOs that Keel et al. (1999) reported (*yellow squares*). East is to the left and north is upward. *Grey shaded regions* correspond to the masked areas. *Black lines* correspond to contours of smoothed LAE number density: $0.5 \times$, $1 \times$ (*solid line*), $2 \times$, and $2.85 \times$ average of the entire field. We call the highest density region as 53W002F-HDR (*orange rectangle*).

be negligible in our sample. Indeed, the previous spectroscopic observations (Matsuda et al. 2005, 2006) show that such contamination in the similar sample at $z = 3.1$ is at most 1%. We ignore the contamination and treat all the 204 objects as LAEs at $z = 2.4$ in the following discussion.

Table 1 shows the properties of these LAEs. We listed not only the results of the fixed aperture photometry but also that of the Kron aperture photometry (SExtractor MAG_AUTO) as many LAEs have the Ly α emission which is more extended than the continuum. Furthermore, we also performed the isophotal photometry for some extended Ly α clouds (i.e. Ly α blobs: LABs), and

their isophotal colors are superposed in Figure 2 (*filled circle*). LABs will be discussed in detail in section 4.1.4.

4. RESULTS

4.1. $z = 2.4$ Galaxies In The Entire Field

4.1.1. Spatial Distribution

The sky distributions of the LAEs in the 53W002 field are shown in Figure 3. The sizes of the symbols represent the rest-frame equivalent width at $z = 2.4$ based on the fixed aperture photometry (large: $EW_0 \geq 200 \text{ \AA}$, middle: $70 \text{ \AA} \leq EW_0 \leq 200 \text{ \AA}$, small: $25 \text{ \AA} \leq EW_0 \leq 70 \text{ \AA}$).

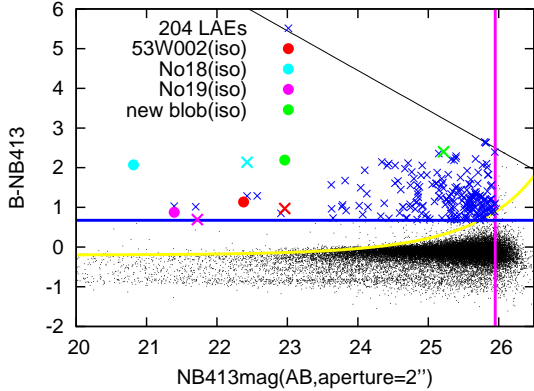


Fig. 2.— The $B - NB413$ versus $NB413$ color magnitude diagram for detected objects in the 53W002 field. The colored lines show the LAE selection criteria: $B - NB413 = 0.68$ (blue line), the 5σ detection limit of the NB413 image (magenta line), and the 4σ color error (yellow curve). Colored crosses show the aperture colors of the selected LAEs; all (blue), 53W002 (red), No.18 (cyan), No.19 (magenta), and LAB4 (green). Filled circles show the isophotal colors for the blobs only, where correspondence between the object and the mark’s color is the same as that of the crosses. The upper bound of the color (black line) corresponds to the 1σ detection limit of the B image.

The contours (black line) show the local surface number density obtained after being smoothed by a Gaussian kernel with $\sigma = 1'.5$ ($0.5 \times$, $1 \times$, $2 \times$, and $2.85 \times$ average value of the entire field are shown). The mean number density of LAEs in the entire field is $0.289 \text{ arcmin}^{-2}$ or $1.16 \times 10^{-3} \text{ Mpc}^{-3}$.

First, we compare our results with the previous LAE search in this field (Pascarelle et al. 1996a,b, 1998; Keel et al. 1999). Figure 4 shows the objects selected as LAEs in Pascarelle et al. (1996b, 1998) and Keel et al. (1999) in our $B - NB413$ versus $NB413$ color magnitude diagram. While the brightest objects and one of the LAEs are recovered in our sample, other objects that have been regarded as LAEs in previous studies are not. Their $B - NB413$ colors are distributed around ~ 0 , which indicates that there is no significant emission line in the narrow-band. This result may be due to the difference of the filters. F410M used

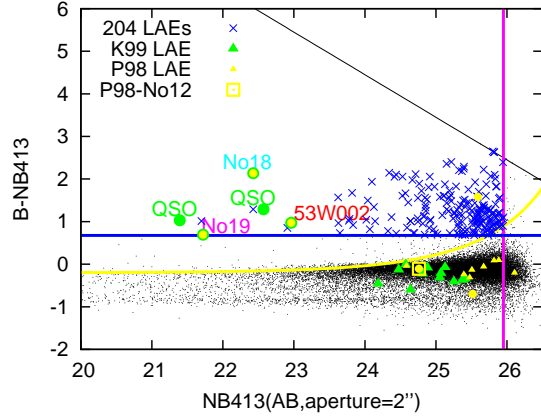


Fig. 4.— The objects previously regarded as LAEs in the $B - NB413$ versus $NB413$ color magnitude diagram. The yellow and green filled triangles represent LAEs in Pascarelle et al. (1998) and Keel et al. (1999), respectively. LAEs that were spectroscopically confirmed as $z \sim 2.4$ are shown by the filled circles. The yellow open square represents P98-No.12 that was spectroscopically confirmed as $z = 2.388$ in Pascarelle et al. (1996b, 1998).

in Pascarelle et al. (1996a,b, 1998) and F413M used in Keel et al. (1999) are medium band filters that have the width of 150 \AA ($FWHM$) in the transmission curve, which samples the LAEs at $z = 2.30 - 2.42$ and $2.32 - 2.45$, respectively. They are about twice as wide as our $NB413$ filter. Among the previously reported LAEs, 10 objects were spectroscopically confirmed as $z \sim 2.4$ (filled circles in Figure 4). 3 AGNs (53W002, No.18 and No.19), 2 QSOs in Keel et al. (1999) and 1 LAE in Pascarelle et al. (1998) (No.29) are also selected in our analysis. No.11 in Pascarelle et al. (1998) is not selected as a LAE, which is naturally understood because its redshift of 2.45 is out of the range of our $NB413$. No.6 in Pascarelle et al. (1998) and No.5 in Keel et al. (1999) locate near bright stars and we masked the field. No.12 in Pascarelle et al. (1996b, 1998) is not selected as a LAE in our analysis while $Ly\alpha$ emission at its redshift of 2.388 should enter the $NB413$ filter (see yellow open square in Figure 4). One possible explanation is that the claimed emission may be a transient such as supernovae at $z = 2.4$, but the reason remains to be unknown.

TABLE 2
SUMMARY OF THE COMPARISON OF LAE NUMBER DENSITIES.

Reference	Field	z	Original criteria ^a ($L: 10^{42} \text{ erg s}^{-1}$) ($EW_0: \text{Å}$)	Matched criteria ^b ($L: 10^{42} \text{ erg s}^{-1}$) ($EW_0: \text{Å}$)	$\bar{n}(\text{field})^c$ (10^{-4} Mpc^{-3})	$\bar{n}(53W002F)^d$ (10^{-4} Mpc^{-3})
Nilsson et al. (2009)	COSMOS	2.25	$L_{NB} \geq 2.7$ $EW_0 \geq 20$	$L_{NB} \geq 2.7$ $EW_0 \geq 25$	4.8 ± 0.3	3.0 ± 0.4
Stiavelli et al. (2001)	DMS 2139-0356	2.4	$L_{Ly\alpha} \geq 2.4$ $EW_0 \geq 25$	$L_{Ly\alpha} \geq 2.4$ $EW_0 \geq 25$	1.3 ± 0.2	2.1 ± 0.3
Prescott et al. (2008)	LABd05	2.7	$L_{NB} \geq 1.7$ $EW_0 \geq 40$	$L_{NB} \geq 1.7$ $EW_0 \geq 40$	19 ± 0.7	4.6 ± 0.5
Guaita et al. (2010)	ECDF-S	2.1	$L_{Ly\alpha} \geq 0.64$ $EW_0 \geq 20$ ^e	...

^aOriginal selection criteria of LAEs in individual studies. Note that they are expressed in our adopted cosmology.

^bMatched LAE selection criteria for the comparison with the number density for the 53W002 field.

^cVolume number densities of LAEs with matched selection criteria for individual fields.

^dVolume number densities of LAEs with matched selection criteria for the 53W002 fields.

^eIt is mentioned that the LAE number density for ECDF-S is roughly the same with that of the $z = 2.25$ LAEs in the COSMOS field.

4.1.2. Number Density of LAEs

In the last section we obtained the LAE average number density in our survey field as $1.16 \times 10^{-3} \text{ Mpc}^{-3}$. This value is estimated for the LAEs with L_{NB} brighter than $1.0 \times 10^{42} \text{ erg s}^{-1}$ and EW_0 larger than 25 Å without correction of the IGM attenuation. We compare the LAE density of the 53W002 field with results of several other $z \sim 2$ LAE studies. Note that the selection criteria as well as the adopted cosmological parameters are matched for the purpose, which is not always straightforward. Nilsson et al. (2009) surveyed the COSMOS field, and obtained a volume density of $6.2 \times 10^{-4} \text{ Mpc}^{-3}$ for $z = 2.25$ LAEs with $L_{NB} \geq 2.3 \times 10^{42} \text{ erg s}^{-1}$ and $EW_0 \geq 20 \text{ Å}$ (in their adopted cosmological parameters). After correcting for the cosmological parameters, the number densities of LAEs with $L_{NB} \geq 2.7 \times 10^{42}$ and $EW_0 \geq 25 \text{ Å}$ are $(3.0 \pm 0.4) \times 10^{-4} \text{ Mpc}^{-3}$ and $(4.8 \pm 0.3) \times 10^{-4} \text{ Mpc}^{-3}$ for the 53W002 field and the COSMOS field, respectively. In the same way we made a comparison with the density of LAEs with $L_{Ly\alpha} \geq 2.4 \times 10^{42} \text{ erg s}^{-1}$ and $EW_0 \geq 25 \text{ Å}$ in Stiavelli et al. (2001). They searched LAEs at $z = 2.4$ in the field around QSO DMS 2139-0356 and showed the volume density of $(1.3 \pm 0.2) \times 10^{-4} \text{ Mpc}^{-3}$. With the same limit,

the volume density for the 53W002 field is estimated as $(2.1 \pm 0.3) \times 10^{-4} \text{ Mpc}^{-3}$. Prescott et al. (2008) studied the overdense environment around a large LAB and found 785 LAEs at $z = 2.7$, which results in the volume density of $(1.9 \pm 0.07) \times 10^{-3} \text{ Mpc}^{-3}$ for the threshold of $L_{NB} \geq 1.7 \times 10^{42} \text{ erg s}^{-1}$ and $EW_0 \geq 40 \text{ Å}$. The density for the 53W002 field is estimated as $(4.6 \pm 0.5) \times 10^{-4} \text{ Mpc}^{-3}$ for the same threshold. The $z = 2.7$ fields clearly has the larger density than our $z = 2.4$ fields. Guaita et al. (2010) surveyed the Extended Chandra Deep Field-South (ECDF-S) and estimated the density of the $z = 2.1$ LAEs as $(3.1 \pm 0.9) \times 10^{-3} \text{ Mpc}^{-3}$. We cannot make a direct comparison as their LAE selection threshold is deeper than ours and there is no catalog of their LAEs. The LAE density for ECDF-S may be comparable or slightly larger than that for the 53W002 field because they mentioned that the density of ECDF-S is roughly the same with that of the $z = 2.25$ LAEs in the COSMOS field (Nilsson et al. 2009). Table 2 summarizes the comparison of the LAE number density of the 53W002 field with that of the four other $z \sim 2$ fields. These comparisons suggest that the LAE volume density in the entire 53W002 field is comparable to those in other $z \sim 2$ general fields.

4.1.3. Sizes and EWs of LAEs

In order to evaluate the size of the Ly α emission, we first made the Ly α image of the LAEs by subtracting the continuum component from the NB413 image. Assuming the flat spectrum of the continuum in the range of B-band, we separated the Ly α component from the continuum component as

$$f_{\nu NB413} = f_{\nu C} + f_{\nu Ly\alpha}, \quad (1a)$$

$$f_{\nu B} = f_{\nu C} + f_{\nu Ly\alpha} \times \frac{\Delta\nu_{NB413}}{\Delta\nu_B}, \quad (1b)$$

where $f_{\nu NB413}$ and $f_{\nu B}$ is the flux per unit frequency ($\text{erg s}^{-1} \text{cm}^{-2} \text{Hz}^{-1}$) for the photons that enter the NB413 and B-band filter, $f_{\nu Ly\alpha}$ and $f_{\nu C}$ is the flux per unit frequency of the Ly α line and the continuum component at the wavelength of 4140 Å, and $\Delta\nu_{NB413}$ and $\Delta\nu_B$ is the width of the NB413 and B-band filter ($FWHM$) in unit of frequency, respectively. We also made the continuum image by subtracting the Ly α component from the B image. The 5σ limiting magnitude in a $2''$ diameter aperture is 26.0 mag for the Ly α image and 26.6 mag for the continuum image. Among the 204 LAEs we carefully selected the objects to measure the sizes which are not easily affected by background noises especially in the continuum image. We made object detection independently on the Ly α and continuum images, and selected the objects that have fluxes brighter than the 2σ detection limit in both images (Ly α < 27.0 mag, continuum < 27.6 mag). This flux criterion is aimed to select objects that have peak higher than twice of the noise, which leads to the robustness in measuring $FWHM$ s of the profiles. The number of objects in the resultant sample is 158, and we used SExtractor to measure their sizes ($FWHM_IMAGE$, $KRON_RADIUS$). Figure 5 shows the size distribution in the Ly α image and the continuum image. The $FWHM$ distributions (*solid line*) suggest that the samples are more extended in Ly α than in continuum, which is a common trend for LAEs (Steidel et al. 2011; Matsuda et al. 2012). There are no notable differences between the $FWHM$ distribution in the 53W002 field and that in another $z \sim 2$ general field reported in Nilsson et al. (2009). We also show the Kron diameter distributions (*dashed line*), which are consistent with the fact that the fluxes using aperture of $2.5 \times$ Kron diameter are

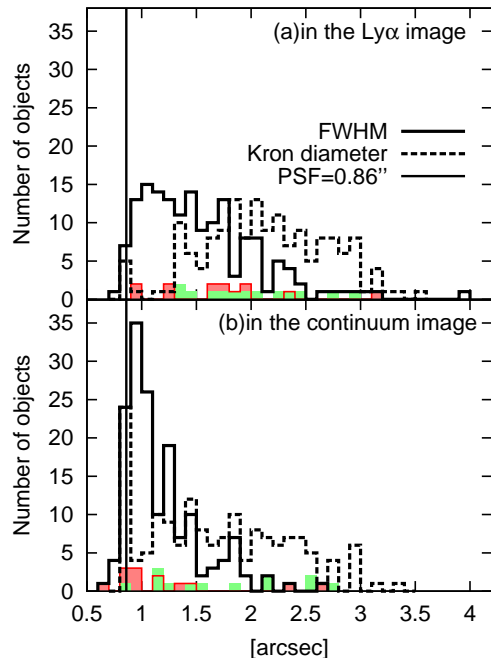


Fig. 5.— The size distribution of the LAEs in the 53W002 field. *Top*: The size in the Ly α image. *Bottom*: The size in the continuum image. In each panel, the *solid black histogram* represents the $FWHM$ distribution of the objects in the entire field, and *red shaded histogram* represents that in 53W002F-HDR. On the other hand *dashed black histogram* and *green shaded histogram* represents the Kron diameter distribution of the objects in the entire field and 53W002F-HDR, respectively. We also show the width of the point sources in $FWHM$, $0.86''$ (*horizontal solid line*).

systematically larger than those using the fixed aperture (see Table 1).

For the EW_0 distribution, it was suggested in previous studies (Gronwall et al. 2007; Nilsson et al. 2007, 2009; Cassata et al. 2011) that the fraction of LAEs with small EW_0 increase at lower redshift. For comparison, we show the distribution of EW_0 of our LAEs in the 53W002 field in Figure 6. Note that these EW_0 are based on the simple calculation assuming neither Galactic nor Intergalactic medium (IGM) extinction. Following Gronwall et al. (2007), we then fitted the EW_0 distribution calculated from the fixed aperture photometry with an exponentially declining

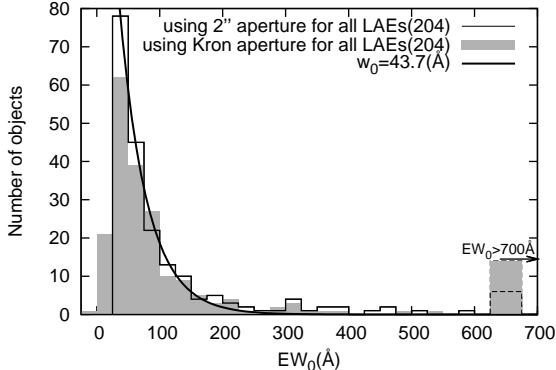


Fig. 6.— The Ly α EW_0 distribution of the 204 LAEs in the 53W002 field. *Solid histogram* shows the EW_0 based on the fixed aperture ($2''$) photometry, and *grey shaded histogram* shows the EW_0 based on the Kron aperture photometry. Bin size is 25 \AA . *Solid curve* indicates the exponential fit to the $2''$ aperture EW_0 distribution. As there are some objects out of the EW_0 range of the figure, we show them in the $EW_0 = 650 \text{ \AA}$ bin.

function:

$$N = C \times e^{-EW_0/w_0}, \quad (2)$$

where C is a normalization constant and w_0 is e-folding length. The best fit solution minimizing the χ^2 is $w_0 = 43.7 \pm 0.43 \text{ \AA}$. While this e-folding length is also slightly smaller than that of $48.5 \pm 1.7 \text{ \AA}$ for $z = 2.25$ LAEs (Nilsson et al. 2009), it is much smaller than that of $76^{+11}_{-8} \text{ \AA}$ for $z = 3.1$ LAEs (Gronwall et al. 2007). It is consistent with the trend that EW_0 distribution becomes narrower at lower redshift. It was also pointed out by the previous studies that the number of LAEs with $EW_0 \geq 240 \text{ \AA}$ is less than that at higher redshift ($z \gtrsim 4$), where such an extremely large EW_0 cannot be explained without top-heavy initial mass function or Population III stars (Malhotra & Rhoads 2002). The fraction of our LAEs that have EW_0 larger than 240 \AA is 0.11 ± 0.02 (23/204) either in the case of $2''$ aperture, or the Kron aperture. This fraction for the 53W002 field is larger than the value, a few percent, for other fields at $z \sim 2$ (Nilsson et al. 2009; Stiavelli et al. 2001). It may be unique property of the 53W002 field that there are substantial number of LAEs that have extremely large EW_0 while the rest distribution is dominated by small EW_0

objects. We also note that there is no notable trend about the sky distribution of high EW objects ($EW_0 > 240 \text{ \AA}$).

4.1.4. Blobs, AGNs and QSOs

There are some unique objects in the 53W002 field. We found four Ly α blobs (LABs), three of which are also reported in previous works. The LABs were selected according to a similar method described in Matsuda et al. (2004). First, we made the object detection on the Ly α image adopting the criteria to have more than 20 contiguous pixels above the threshold of 2σ of the background fluctuation, which corresponds to $27.1 \text{ mag arcsec}^{-2}$ ($7.90 \times 10^{-18} \text{ erg s}^{-1} \text{ cm}^{-2} \text{ arcsec}^{-2}$). Next, the $NB413$ and B magnitudes of the detected objects were measured using the same isophotal apertures defined in the process of source detection on the Ly α image. We then selected the LABs by adopting the following criteria. (i) $NB413 - B(\text{isophotal}) \geq 0.68$ & $NB413(\text{isophotal}) \leq 25.95$: these are the criteria to select emitters. (ii) Isophotal area in the Ly α image $\geq 10 \text{ arcsec}^2$: the threshold of 10 arcsec^2 corresponds to the area of a circle with a diameter of 30 kpc in physical scale at $z = 2.4$. We refer to the detected four LABs as 53W002 (LAE145), No.18 (LAE14), No.19 (LAE201) which are named according to the previous works (Windhorst et al. 1991; Pascarelle et al. 1996b), and LAB4 (LAE4) which was newly found in this study.

The properties of the four LABs (including the isophotal $B - NB413$ colors) are shown in Table 3 and Figure 2 (*filled circles*). In Table 3 we show not only the isophotal areas but also the major-axis diameters (Matsuda et al. 2011). The $NB413$, B , Ly α and continuum images of the four LABs are shown in Figure 7, where the 2σ isophotal apertures of the Ly α image that we used in both of the detection and photometry are superposed on the continuum images. 53W002, which is originally found as a weak radio source (Windhorst et al. 1991), has the smallest isophotal area and major-axis among the four LABs.

No.18 lies in the northwest direction from 53W002, and it is the most unique object with several very interesting features. First it is notable that No.18 has an extremely large EW_0 and very extended Ly α nebulae in spite of a substantial amount of dust (see later description). We

TABLE 3
 PROPERTIES OF THE LABS IN THE 53W002 FIELD

ID	R.A.	Dec.	Area ^a	a^b	EW_0^c	$\log L_{Ly\alpha}^c$	$\log(SB)^d$	Note	Ref
(1)	(deg) (2)	(deg) (3)	(arcsec ²) (4)	(kpc) (5)	(iso, Å) (6)	(iso, erg s ⁻¹) (7)	(erg s ⁻¹ cm ⁻² arcsec ⁻²) (8)	(9)	(10)
53W002 (LAE145)	258.56128	50.25853	16.32	59.3	59.3	43.294	-16.592	radio	1
No.18 (LAE14)	258.55016	50.26759	61.6	93.3	325	44.037	-16.425	AGN/QSO	2,3
No.19 (LAE201)	258.54727	50.26960	19.28	88.5	37.4	43.620	-16.338	QSO	2
LAB4 (LAE4)	258.54414	50.39581	25.8	90.4	439	43.185	-16.899

^aIsophotal area above 2σ arcsec⁻² of the background fluctuation of the Ly α image.

^bMajor-axis diameter of the isophotal aperture in physical scale at $z = 2.4$.

^cThe sixth and seventh rows are based on the isophotal aperture photometry.

^dAverage Ly α surface brightness.

References. — (1) Windhorst et al. 1991; (2) Pascarella et al. 1996b; (3) Smail et al. 2003.

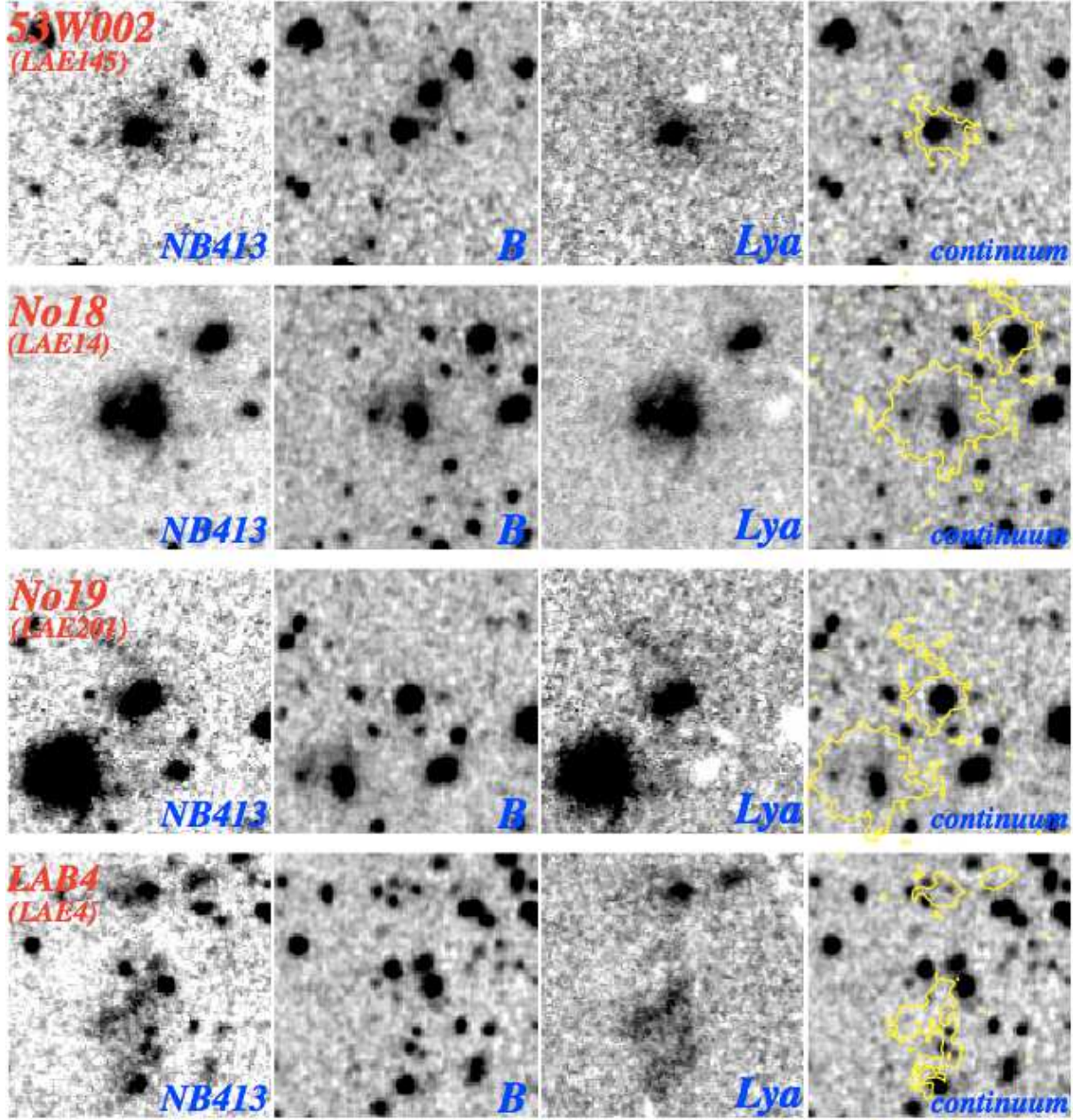


Fig. 7.— *B*, *NB413*, *Ly α* , and continuum images of the 4 LABs in the 53W002 field. North is up, and each panel's size is 24×24 arcsec 2 which corresponds to 200×200 kpc 2 in physical scale. *Yellow contours* superposed on continuum images show the isophotal apertures of the *Ly α* image, 2σ arcsec $^{-2}$ of the background fluctuation (7.90×10^{-18} erg s $^{-1}$ cm $^{-2}$ arcsec $^{-2}$).

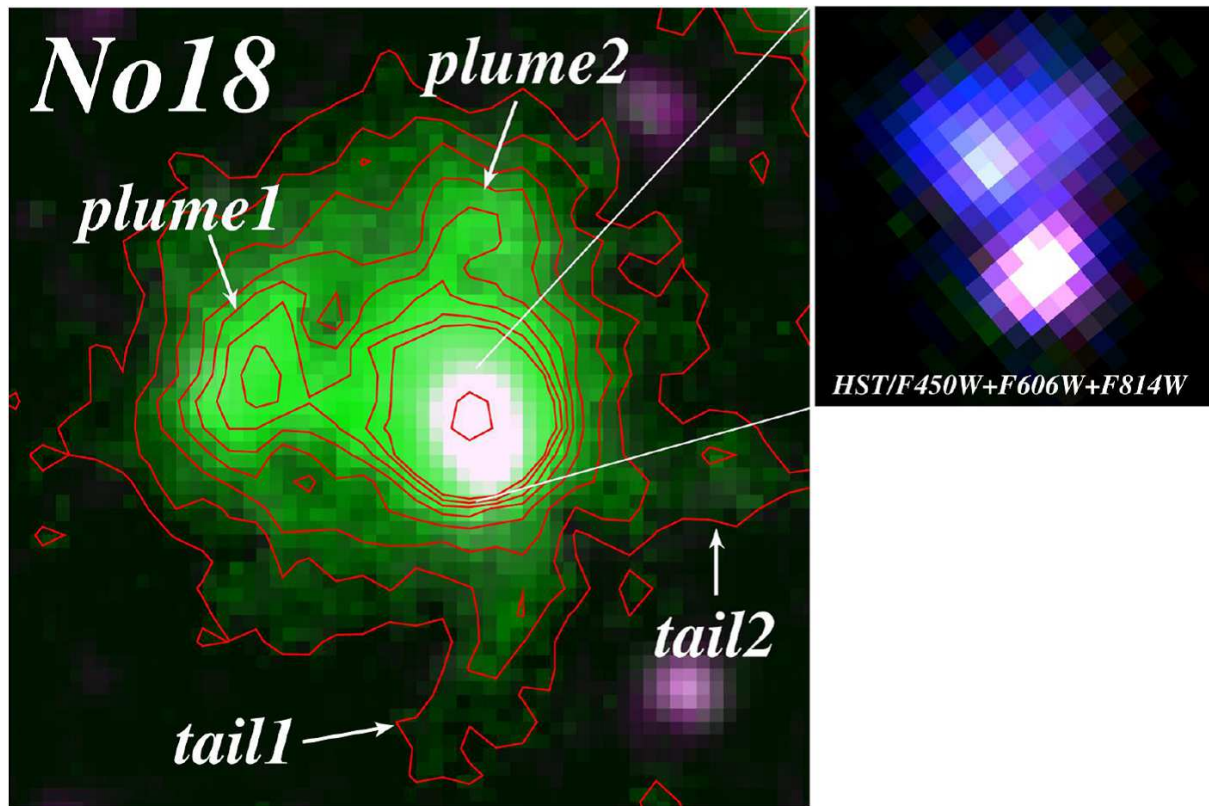


Fig. 8.— Pseudo-color images of No.18 whose color consists of $NB413$ for green, and B for blue and red (the left big panel). The panel’s size is $12 \times 12 \text{ arcsec}^2$ which corresponds to $100 \times 100 \text{ kpc}^2$ in physical scale. *Red lines* superposed on the image correspond to the isophotal contours of the $\text{Ly}\alpha$ image at levels of 2, 4, 6, 8, 10, 12, 14, 16, and $100\sigma \text{ arcsec}^{-2}$. The small right panel is the enlarged image of the central core. Colors are F450W for blue, F606W for green, and F814W for red. The panel’s size is $2 \times 2 \text{ arcsec}^2$ (physical $17 \times 17 \text{ kpc}^2$).

show the pseudo-color image of No.18 ($NB413$ for green, B for blue and red) as well as their $\text{Ly}\alpha$ surface brightness in Figure 8. It clearly has two bright structures in $\text{Ly}\alpha$ (*plume1* and *plume2*). The unique shape of *plume1* appears like a bow-shock front with a jet expelled from the core. A weak continuum source is seen in the $\text{Ly}\alpha$ isophotal contour of *plume1*, although there is a small offset between their positions. No.18 also has two tails with lower surface brightness (*tail1* and *tail2*). They resemble tidal tails, which may indicate that No.18 is undergoing a merger process. On the other hand, *tail1* and *tail2* are seen only in the $\text{Ly}\alpha$ image and no significant continuum emission is detected. If these tails consist only of gas and not of stars the energy source

of $\text{Ly}\alpha$ emission remains to be considered. In Figure 8 we also show the enlarged image of the central core that is unresolved in our continuum image but resolved in *HST* images. Note that we used the *HST* archive data (WFPC2/F450W, F606W, and F814W) to make the color image, which are the same as that used in the previous study (Pascarelle et al. 1996b). The core consists of two components: the compact southern component that has redder color in the rest-frame optical/UV, and the more diffuse northern component that even has bluer color and weaker continuum brightness, though a large fraction of the $\text{Ly}\alpha$ emission comes from this component (Smail et al. 2003). Near-infrared spectroscopy classified the southern component as a Seyfert 2

AGN (Motohara et al. 2001a). Smail et al. (2003) discovered the submillimeter counterpart (SMG) to No.18. They also summarized several studies about No.18 that its physical process may be the complex mix of star formation, AGN activity of the southern component, resulting local ionization or illumination of the northern component and extended superwind driven by highly obscured starburst. Our results are well consistent with their picture about the core as the northern component has a large fraction of Ly α (see the 100 σ isophotal contour in Figure 8). *Plume1* appears to be expelled from the northern component, which is consistent with the appearance of the high spatial resolution Ly α image by *HST* (see Smail et al. 2003). Further observation, especially for *plume1* and the northern component that have never been observed spectroscopically, is needed in order to get a definitive picture about the physical process occurred in No.18.

No.19, which lies close by No.18, was found as a variable QSO and spectroscopically confirmed to be at $z = 2.397$ (Pascarelle et al. 1996a). In the Ly α image it shows faint and clumpy tails that is detected for the first time. Including the tails we estimated the size as 88.5 kpc in physical scale, which is relatively large among the LABs in other fields. Unlike No.18, however, we consider that No.19 is physically dominated by AGN because of its small EW_0 .

LAB4 (the south object of the bottom row in the stamps in Figure 7) is located in the region previously not observed and with two blobby companions in the north. Unlike the other three objects associated with AGNs, LAB4 has no strong continuum counterpart and looks filamentary in Ly α .

We also detected two QSOs previously reported (Keel et al. 1999) as LAEs (called as LAE77 and LAE128). LAE128 is located at the peak of the smoothed LAE number density in the 53W002 field, and LAE77 is also at relatively higher density region (see *yellow squares* in Figure 3).

4.2. 53W002F-HDR

The most dense part in our surveyed field is at around $(\alpha, \delta) = (17^h 14^m 10^s.0, +50^\circ 17' 30'')$ where the local number density is ~ 2.9 times of the average of the entire field. We identify the $4.7' \times 4.1'$ region around the most dense point as the high

density region and refer this as 53W002F-HDR (see the *orange rectangle* in Figure 3). 53W002F-HDR has a volume of 4850 Mpc³ in comoving scale and the LAE total number of 21. So the mean number density of the 53W002F-HDR is 4.33×10^{-3} Mpc⁻³, which is nearly four times as large as the mean of the entire field. The four unique objects (53W002, No.18, No.19 and LAE128) lie in the very small volume of 53W002F-HDR. In Figure 5 the *FWHM* (*red shaded*) and Kron diameter (*green shaded*) distributions of the LAEs in 53W002F-HDR are presented.

5. DISCUSSION

5.1. Rareness Probability of 53W002F-HDR

In this section we are going to discuss how significant 53W002F-HDR is. We should apply a more objective indicator of the significance of the structure than just density so that we can also make comparison with proto-cluster regions at other redshift and to trace the evolution of galaxies in such dense environment. We introduce a new quantity for this purpose.

Assuming the number density of the LAEs in the entire survey field as the average in the $z = 2.4$ universe ($\bar{n} = 1.16 \times 10^{-3}$ Mpc⁻³), the number density of 53W002F-HDR ($n_{HDR} = 4.33 \times 10^{-3}$ Mpc⁻³) is converted to the LAE overdensity,

$$\delta_{LAE,HDR} = \frac{n_{HDR} - \bar{n}}{\bar{n}} = 2.7 \pm 0.8, \quad (3)$$

where the error is the poisson error. Although this represents the overdensity of the LAE number density, we assume this can be regarded as the LAE mass overdensity, $(\rho_{HDR} - \bar{\rho})/\bar{\rho}$. Furthermore we approximated the overdensity of the underlying mass assuming the LAE linear bias by

$$\delta_{LAE} = b_{LAE} \times \delta_{mass}. \quad (4)$$

There is only a few studies about bias for $z \sim 2$ LAEs and almost all of them estimated linear bias. So we used the linear bias of $b_{LAE} = 1.8 \pm 0.3$, which was estimated from the observation of 250 LAEs at $z = 2.1$ (Guaita et al. 2010). Thus, the mass overdensity of 53W002F-HDR results in $\delta_{mass,HDR} = 1.5 \pm 0.5$.

Then we introduce the probability distribution function (PDF) to characterize the general distribution of mass fluctuations in the specific red-

shift universe. By definition, the PDF of cosmological density fluctuations describes the probability of having a fluctuation in the overdensity range $(\delta, \delta + d\delta)$, within a spherical region of characteristic radius R randomly located in the universe at the given redshift. We followed mainly Marinoni et al. (2005, 2008) to make the PDF of the underlying mass theoretically. Its shape is well approximated by a lognormal distribution up to moderately non-linear regimes (Coles & Jones 1991; Kofman et al. 1994; Taylor & Watts 2000; Kayo et al. 2001),

$$f_R(\delta) = \frac{(2\pi\omega_R^2)^{-1/2}}{1+\delta} \exp\left[-\frac{\{\ln(1+\delta) + \omega_R^2/2\}^2}{2\omega_R^2}\right]. \quad (5)$$

This formula is fully characterized by a single parameter ω_R , which is related to the variance of the overdensity field on the scale R ($\sigma_R^2 \equiv \langle \delta^2 \rangle_R$) as

$$\omega_R^2 = \ln(1 + \sigma_R^2). \quad (6)$$

The linear growth theory approximation is used to estimate $\sigma_R(z)$ with the normalization factor of $\sigma_8 = 0.81$ (Komatsu et al. 2011). We applied the correction of the redshift distortion to $\sigma_R(z)$ in Eq.(6) because we need to make the PDF in redshift space in order to compare with the observations. The correction accounts for the average contribution of the linear redshift distortions induced by peculiar velocities (Kaiser 1987). See Marinoni et al. (2005) for more details. Figure 9 shows the examples of the PDF of mass fluctuations for three different epochs, where we adopt the radius of sampling spheres of $R = 10$ Mpc. We also attempt to reconstruct mass PDF from the observed LAE distribution. First, we measured the LAE overdensities within a circular regions with the radius of $2.3'$ (comoving 3.9 Mpc) randomly located in the field except for the edge. These circular regions have the equivalent volume with spheres with radius of 10 Mpc. Next, we assume the linear bias ($b_{LAE} = 1.8$) to convert the LAE overdensities to mass overdensities. The resulting mass PDF is shown in Figure 9 (*grey shaded histogram*). The theoretical and observed PDFs of mass fluctuation at $z = 2.4$ seem to be in reasonably good agreement. A Kolmogorov-Smirnov (KS) test gives the significance probability of the difference between the two distributions (KS probability, ranging between 0 and 1), 0.99.

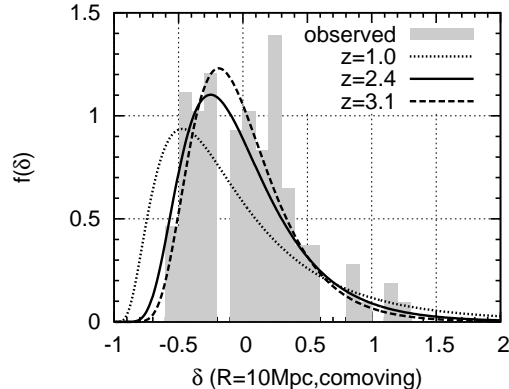


Fig. 9.— The PDF of mass fluctuations with the scale of $R = 10$ Mpc for three different cosmic epochs: $z = 1.0$ (*dotted curve*) simply for a comparison, $z = 2.4$ (*solid curve*) that is the epoch we observe in this study, and $z = 3.1$ (*dashed curve*) that is the epoch of the supplement data noticed in Section 5.2. They are predicted theoretically from Eq.(5). We also show the mass PDF obtained observationally from the data of LAEs at $z = 2.4$ in the 53W002 field (*grey shaded histogram*), where we used the linear bias to convert the LAE overdensity to the mass overdensity (see text for details). A KS test does not reject the null hypothesis that the observed mass PDF is drawn from the theoretical PDF at $z = 2.4$ (KS probability = 0.99).

We evaluated the significance of 53W002F-HDR as follows. First we made the theoretical mass PDF at $z = 2.4$ with $R = 10.5$ Mpc, this scale corresponds to the radius of a sphere having the equivalent volume with 53W002F-HDR in comoving scale. Next we calculated the probability of having δ_{mass} larger than that of 53W002F-HDR (1.5 ± 0.5) from the mass PDF, $0.9^{+2.4}_{-0.62}\%$. This implies that 53W002F-HDR is a rich region in the $z = 2.4$ universe where such overdense structure exist with the probability of $\sim 0.9\%$. Hereafter we call the probability representing rareness of structure as “rareness probability”.

Next, we compare the rareness probability of 53W002F-HDR with those of other high density regions traced by LAEs at $z > 2$. For comparison, we used the data of the SSA22 field at $z = 3.1$ (Yamada et al. 2012), the TN J1338-1942 field at $z = 4.1$ (Venemans et al. 2002), and the

6C0140+326 field at $z = 4.4$ (Kuiper et al. 2011), where their comoving volumes and LAE overdensities are available. The central region in the SSA22 field (Sb1 peak) has comoving volume of 20,580 Mpc^3 and LAE overdensity of 3.36 ± 0.03 . We calculated the rareness probability of the Sb1 peak assuming LAE linear bias of 1.9 (Guaita et al. 2010), which results in the rareness probability of $0.0017^{+0.0002}_{-0.0001}\%$. The region around the radio galaxy TN J1338-1942 has comoving volume of 7,315 Mpc^3 and LAE overdensity of 4 ± 1.4 , whose rareness probability is $0.2^{+1.5}_{-0.17}\%$ assuming the LAE linear bias of 3.7 (Kovač et al. 2007). The comoving volume and LAE overdensity of the region around the radio galaxy 6C0140+326 is 1570 Mpc^3 and 8 ± 5 , respectively. This corresponds to the rareness probability of $0.043^{+3.49}_{-0.042}\%$, where we assume that the LAE linear bias is 3.7 (Kovač et al. 2007). Compared with these values, the rareness probability of 53W002F-HDR, 0.9%, is larger or less significant. We also estimated the descendant of 53W002F-HDR in local. The galaxy overdensity of the spherical region at $z = 0$ which have the same comoving volume and the same rareness probability with 53W002F-HDR is found to be ~ 4 , assuming that galaxy bias is unity ($b = 1$). Following Croton et al. (2005) where clusters are defined as structures whose overdensity of galaxies within $8 h^{-1}$ Mpc sphere (δ_8) is larger than 6.0, the structure whose δ_8 equals to 4 (rareness probability $\sim 0.9\%$) is not classified as a cluster although it is significant high density region. On the other hand, it is difficult to find one-to-one correspondence between the regions with similar rareness probability at $z = 2.4$ and $z = 0$ because the non-linear effects should be much more seriously considered at lower redshift. Therefore we only argue that 53W002-HDR may not evolve to extremely prominent rich cluster at $z = 0$.

5.2. The Environmental Dependency of LAEs' Properties

In order to discuss the properties of LAEs as a function of the local density environment, we evaluated the LAE overdensities in circular regions with the radius of $2.3'$ centered at each LAE, which corresponds to the volume of a sphere with radius of 10 Mpc. Here we used the 162 LAEs that lie at least $2.3'$ away from the edge of the image to avoid the edge effect.

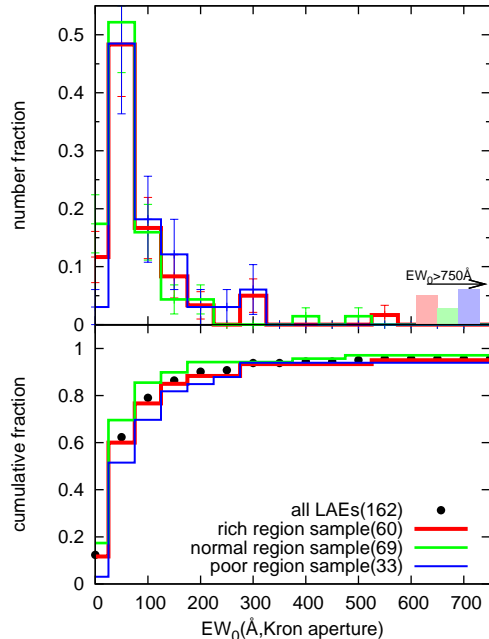


Fig. 10.— The $\text{Ly}\alpha$ EW_0 distributions in the 53W002 field for the three subsamples divided by their LAE number overdensities: the rich region sample (red histogram), the normal region sample (green histogram), and the poor region sample (blue histogram). The differential (top panel) and cumulative (bottom panel) distributions are shown, and the objects out of the EW_0 range of the figure are also shown (shaded boxes in top panel).

To search for the dependence of the properties on the environment for the 162 LAEs in the 53W002 field, we divided the samples into the three subsamples with LAE overdensity, $\delta_{LAE} = 0.94$ and -0.17 , which correspond to the rareness probabilities of 12% and 50%. Hereafter we call the subsample with the LAE overdensity range of $-1 \sim -0.17$, $-0.17 \sim 0.94$ and $0.94 \sim$ as the “poor region sample”, the “normal region sample” and the “rich region sample”, respectively. They contain 60, 69, and 33 LAEs. First, we investigated the EW_0 distributions. Here we used the EW_0 measured by the Kron photometry to capture the scattered component of $\text{Ly}\alpha$ emission while it actually gives the lower limit, as the EW_0 may be affected by possible contamination of the foreground galaxies in the continuum. Figure 10 shows the obtained differential (top) and cumulative (bottom)

distributions of the three subsamples. There is no notable difference among the three subsamples. A KS test shows that every two subsamples have similar distributions with the KS probability larger than 0.25. We also found that there is no notable difference in the number fraction of LAEs with EW_0 larger than 240 \AA : 0.12 ± 0.04 for the rich region sample, 0.06 ± 0.03 for the normal region sample, and 0.15 ± 0.07 for the poor region sample. Next, we investigated the distributions of the $\text{Ly}\alpha$ luminosities. We show the result in Figure 11. The distributions of the three subsamples seem to be in agreement within the error bars. There may be a possible weak trend that the rich region sample has a distribution biased to larger $\text{Ly}\alpha$ luminosities than others. The difference between the rich region sample and others, however, is not significant with KS probability of $\gtrsim 0.5$. It is expected that the $\text{Ly}\alpha$ luminosity and EW_0 are connected with a mechanism emitting $\text{Ly}\alpha$ photons of LAEs. In this sense, the $\text{Ly}\alpha$ emitting mechanism of LAEs does not depend on their environment (10Mpc scale) at least in the 53W002 field.

We also investigated the environmental dependency of LAEs in other fields for comparison. As supplemental data, 386 LAEs in the SXDS field and 196 LAEs in the SDF field at $z = 3.1$ are used from the sample in Yamada et al. (2012). In their analysis, the SXDS and SDF fields are considered as the blank fields at $z = 3.1$ with no significant density excess. Before discussing the environmental dependency, we investigated the $\text{Ly}\alpha$ EW_0 and luminosity distributions of whole sample in the $z = 3.1$ blank field. For the EW_0 distribution, we fitted it with an exponentially declining function (Eq.(2)) and derived the best fit solution of $w_0 = 64.4 \pm 1.5 \text{ \AA}$. This e-folding length at $z = 3.1$ is significantly larger than $w_0 = 43.7 \pm 0.43 \text{ \AA}$ of the 53W002 field at $z = 2.4$, and this trend is consistent with the discussion in section 4.1.3. On the other hand, we found no notable evolution of $\text{Ly}\alpha$ luminosity distribution although the difference of completeness makes the comparison not straightforward. In order to search for environmental dependency, we applied almost the same procedure as we did for the LAEs in the 53W002 field: counting the number within the circular region that has the equivalent volume with a sphere with radius of 10 Mpc in comoving scale, rejecting the samples

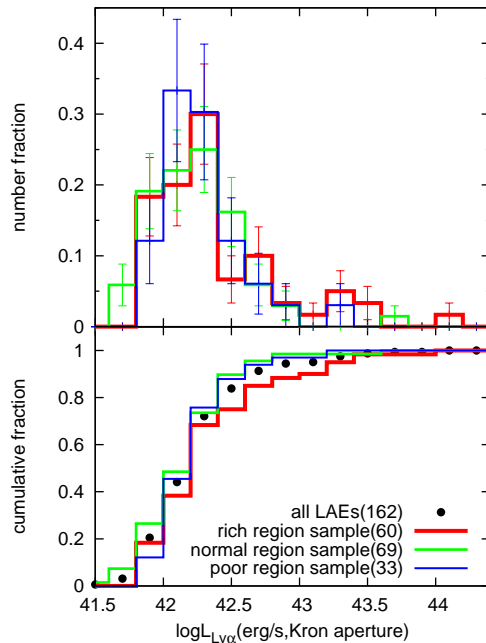


Fig. 11.— The $\text{Ly}\alpha$ luminosity distributions in the 53W002 field for the three subsamples, where we use the same relation between color of histograms and subsamples with Fig 10.

near the edge of the images, dividing the samples into the three subsamples (the rich, normal and poor region sample), and using the measurements based on the Kron photometry. To match the $z = 3.1$ subsamples with that at $z = 2.4$, we used the rareness probability scaled by redshift instead of the observed surface density. That is, we adopted the rareness probabilities of 12% and 50% as the separators of the subsamples for the total of 440 LAEs in the $z = 3.1$ blank fields, where we used the LAE bias of $b_{LAE} = 1.9$ (Guaita et al. 2010). This corresponds to the LAE number overdensity of 0.85 and -0.13. In Figure 12 we summarize the results of our analysis for the $z = 3.1$ blank fields. KS probabilities for every two subsamples are at least larger than 0.21 in EW_0 distributions, and at least larger than 0.34 in $L_{\text{Ly}\alpha}$ luminosity distributions. There seems to be no dependence of the EW_0 or $\text{Ly}\alpha$ luminosity distributions on environment in the $z = 3.1$ blank fields. This is consistent with the results in the 53W002 field, and it may be the general property of LAEs. We expected that the external environmental effects

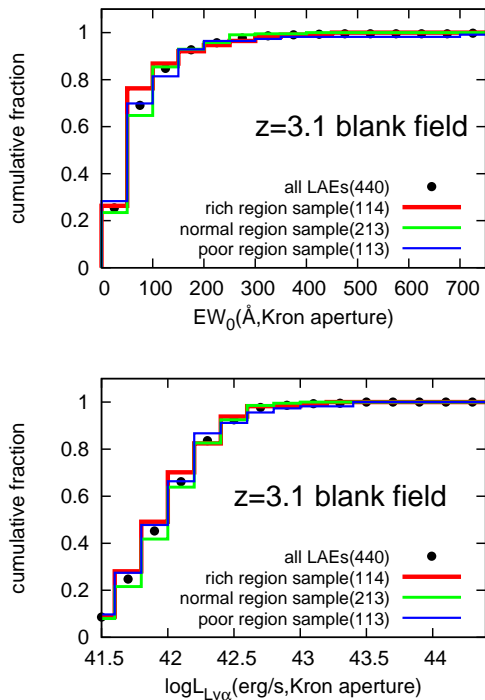


Fig. 12.— The $\text{Ly}\alpha$ EW_0 (*top panels*) and luminosity (*bottom panels*) distributions for the $z = 3.1$ blank fields (the SXDS field and the SDF field). The LAEs are divided into the three subsamples (see text) and the numbers contained in each subsample are shown in the parentheses of each legend. We rejected the objects near the edge of the images from the original catalog (Yamada et al. 2012).

such as ram pressure, tidal stripping, harassment and so on (which work in timescales of \sim a few Gyr in typical clusters) are not effective because LAEs are thought to be young galaxies (typically have age $\sim 10^7$ yr). The results revealed in this section suggest that the intrinsic environmental effects such as galaxy formation bias does not affect the properties of the $\text{Ly}\alpha$ emission of LAEs, at least at the scale of 10 Mpc. It is also interesting that EW distribution of LAEs changes only along redshift. If the EW evolution along redshift is due to evolution of dust amount as claimed in the previous studies (Nilsson et al. 2009), there should also be environmental dependency since metal enrichment is expected to be proceeded more quickly in high density environment. So far there is no

definitive answer for this question, but we consider that such environmental information is a key to understand the evolution of LAEs.

5.3. Rich Regions and LABs

About the four LABs in the 53W002 field we found that they have almost the same rareness probabilities: No.18 and No.19 have 7.7%, and 53W002 and LAB4 have 10.2%. This clearly supports the view that LAB is a population biased to high density environment (Steidel et al. 2000; Matsuda et al. 2004; Prescott et al. 2008). Interestingly the rareness probabilities of the LABs in the 53W002 field imply that they are not biased to the most dense region but more located at moderate density regions such as the rim of 53W002F-HDR. Especially for No.18 and No.19, we consider that galaxy - galaxy mergers may have triggered their AGN activity and induced their morphological features like tail or jet because the merging mechanism becomes effective in outer regions of clusters of galaxies at least in the local universe (Treu et al. 2003). The *HST* images of No.18, which shows the double component having different colors and $\text{Ly}\alpha$ brightness in the core unresolved in our images, strengthen the merging hypothesis. No.19, which lies at the distance of only 80 kpc (physical) from No.18, can be considered as to interact with No.18. Unlike the other three, LAB4 doesn't have a strong continuum counterpart such as a QSO, AGN and radio galaxies and looks filamentary. Besides, only LAB4 lives far outside 53W002F-HDR. It lies with a little offset from the local density peak as the other three did, and possibly interacts with the two blobby LAEs located in the north of LAB4 (see Figure 7). We speculate that the merger scenario may play a key role in the formation of LABs, but it is needed to confirm the trend that LABs have moderate small rareness probabilities using much larger samples in order to obtain the conclusion.

6. CONCLUSION

We conducted the deep and wide-field imaging of the 53W002 field.

From the spatial distribution of the 204 LAEs in the 53W002 field at $z = 2.4$ we identified the overdense region named 53W002F-HDR, where 53W002 lies at the rim. It is found that 53W002F-

HDR is a moderately rich region in the $z = 2.4$ universe where such overdense structure exist with the rareness probability of $\sim 0.9\%$. The results of the analysis to search for environmental dependency of the properties of LAEs (i.e. Ly α luminosity and EW_0) shows that the physical process of emitting Ly α photons of LAEs does not depend on the local density environment at least for 10 Mpc scale. This is in contrast to the fact that the EW_0 distribution changes along redshift. On the other hand, the four LABs (53W002, No.18, No.19 and LAB4) are clearly biased to a moderately rich region such as the rims of the density peaks. This trend may give some hints about the origin of the morphological uniqueness of the LABs.

We thank the staff of the Subaru Telescope for their assistance. This research is supported in part by the Grant-in-Aid 20450224 for Scientific Research of the Ministry of Education, Science, Culture, and Sports in Japan.

Facilities: National Astronomical Observatory of Japan (NAOJ).

TABLE 1
 PROPERTIES OF THE LAES IN THE 53W002 FIELD

53W002F- LAE#	R.A. (deg)	Dec. (deg)	EW_0^a ($2''$, Å)	EW_0^b (Kron, Å)	$\log L_{Ly\alpha}^a$ ($2''$, erg s $^{-1}$)	$\log L_{Ly\alpha}^b$ (Kron, erg s $^{-1}$)	Local density ^c (arcmin $^{-2}$)	z_{spec}	Note	Ref
(1)	(2)	(3)	(4)	(5)	(6)	(7)	(8)	(9)	(10)	(11)
1	258.63076	50.16096	7940	40900	42.073	42.085	0.183
2	258.42144	50.25102	5310	∞	42.065	42.234	0.385
3	258.57732	50.30839	4970	1500	42.064	42.011	0.774
4	258.54392	50.39660	865	134	42.295	43.264	0.589	...	LAB(newly found)	...
5	258.54149	50.39972	723	48.3	42.32	42.671	0.589
6	258.54364	50.39938	310	82.1	42.595	43.062	0.589
7	258.44731	50.45681	838	11500	42.004	42.077	0.376
8	258.72317	50.32180	582	97.5	42.218	42.296	0.496
9	258.97269	50.41476	500	1060	42.217	42.243	0.0764
10	258.59804	50.35524	474	2630	42.104	42.135	0.561
11	258.18753	50.29742	454	∞	42.241	42.464	0.187
12	258.78259	50.29046	426	45.7	42.223	42.261	0.63
13	258.62255	50.37131	386	285	42.631	42.676	0.568
14	258.55015	50.26760	379	312	43.397	44.066	0.694	2.393	LAB/SMG/AGN(No.18)	2,3,5,6
15	258.58318	50.32840	360	203	42.48	42.808	0.705
16	258.42732	50.22930	351	495	42.589	42.687	0.443
17	258.53700	50.40982	347	312	42.034	42.282	0.607
18	258.54341	50.28229	320	995	42.054	42.142	0.789
19	258.76163	50.39229	314	528	42.55	42.619	0.678
20	258.40484	50.16364	314	313	42.396	42.424	0.21
21	258.49734	50.12923	283	966	42.024	42.115	0.21
22	258.79474	50.21872	264	941	42.489	42.603	0.466
23	258.44204	50.33868	242	295	42.714	42.805	0.248
24	258.78261	50.07203	237	338	42.13	42.246	0.155
25	258.84603	50.14729	221	379	42.443	42.532	0.476
26	258.54748	50.42515	216	1630	42.064	42.23	0.524
27	258.22744	50.28924	216	243	42.297	42.327	0.161
28	258.53390	50.32310	196	148	42.229	42.211	0.592
29	258.66347	50.22008	195	162	42.001	41.984	0.277
30	258.74374	50.25124	193	103	42.004	42.199	0.422
31	258.48470	50.27243	193	31.7	42.351	42.333	0.528
32	258.88279	50.11165	188	53.3	42.382	42.481	0.371
33	258.66246	50.38647	171	204	42.154	42.246	0.716
34	258.53123	50.28973	162	151	42.257	42.37	0.817
35	258.57848	50.44524	161	171	42.415	42.526	0.322
36	258.49930	50.30915	155	142	42.089	42.122	0.557
37	258.20361	50.43484	148	106	42.8	42.879	0.141
38	258.34411	50.34501	145	137	42.499	42.556	0.188
39	258.27613	50.18828	136	115	42.239	42.264	0.103
40	258.91993	50.24691	132	95	42.509	42.767	0.318
41	258.75740	50.36116	132	24.7	42.274	42.209	0.716
42	258.69606	50.39156	131	96.8	42.039	42.108	0.754
43	258.21611	50.19650	131	119	42.277	42.364	0.0995

TABLE 1—*Continued*

53W002F- LAE# (1)	R.A. (deg) (2)	Dec. (deg) (3)	EW_0^a ($2''$, Å) (4)	EW_0^b (Kron, Å) (5)	$\log L_{Ly\alpha}^a$ ($2''$, erg s $^{-1}$) (6)	$\log L_{Ly\alpha}^b$ (Kron, erg s $^{-1}$) (7)	Local density ^c (arcmin $^{-2}$) (8)	z_{spec} (9)	Note (10)	Ref (11)
44	258.41791	50.40316	128	138	42.086	42.188	0.347
45	258.57892	50.27311	125	113	42.081	42.138	0.652	2.396	...	4
46	258.93658	50.17620	125	62.7	42.295	42.418	0.204
47	258.75387	50.37258	123	113	42.867	42.982	0.754
48	258.45500	50.41545	123	181	41.955	41.993	0.504
49	258.52829	50.12714	122	216	42.24	42.372	0.203
50	258.59951	50.14995	122	151	42.377	42.519	0.176
51	258.81284	50.23541	120	80.2	42.416	42.513	0.478
52	258.44835	50.39939	117	127	41.957	42.076	0.424
53	258.84204	50.15028	113	24.6	42.359	42.301	0.484
54	258.59013	50.21903	113	125	42.147	42.221	0.257
55	258.24914	50.09305	109	70.7	42.691	42.739	0.259
56	258.73629	50.28981	109	106	42.153	42.217	0.59
57	258.87868	50.41749	106	48.2	42.218	42.223	0.123
58	258.82293	50.10331	100	96.5	42.456	42.504	0.389
59	258.85402	50.30794	100	80.7	42.112	42.24	0.484
60	258.24106	50.11929	98.3	204	42.237	42.413	0.287
61	258.24326	50.44970	98.2	95.6	42.079	42.163	0.233
62	258.35531	50.42865	97.8	362	42.125	42.419	0.272
63	258.73028	50.15968	93.5	88.1	41.958	42.143	0.148
64	258.83270	50.19312	91.9	82.6	42.152	42.252	0.454
65	258.34519	50.33534	91.8	71.2	42.35	42.443	0.188
66	258.73498	50.37537	90.7	55.1	42.02	42.006	0.772
67	258.78771	50.34518	89.7	76.6	42.027	42.201	0.581
68	258.94266	50.21324	84.6	190	42.119	42.415	0.22
69	258.19161	50.10535	84.3	105	42.633	42.767	0.225
70	258.86881	50.08927	83.3	130	42.153	42.234	0.294
71	258.43415	50.25486	82.9	65.4	42.01	42.014	0.453
72	258.95865	50.14175	82.6	55.9	42.341	42.591	0.139
73	258.33629	50.43656	81.1	44.1	42.011	42.015	0.32
74	258.68497	50.41743	80.6	145	42.034	42.158	0.411
75	258.15448	50.40201	78.3	80.9	41.981	42.029	0.0888
76	258.53214	50.27693	78.2	62.9	42.086	42.249	0.74
77	258.55175	50.30537	76.8	79	43.246	43.302	0.814	2.381	QSO	5
78	258.38775	50.10565	76.5	77.5	43.303	43.354	0.211
79	258.65633	50.30749	76.3	51	42.027	41.975	0.525
80	258.43633	50.17643	76.2	96.7	42.213	42.493	0.357
81	258.45001	50.24254	76.1	14.3	41.984	41.651	0.493
82	258.31564	50.43478	74.8	1240	42.152	42.418	0.331
83	258.69831	50.22212	74.2	59.9	41.962	42.03	0.25
84	258.62737	50.34087	73.9	173	42.01	42.254	0.651
85	258.44133	50.45587	73.8	11.8	42.02	41.816	0.363
86	258.76886	50.36924	73.1	76	42.066	42.245	0.701

TABLE 1—*Continued*

53W002F- LAE# (1)	R.A. (deg) (2)	Dec. (deg) (3)	EW_0^a ($2''$, Å) (4)	EW_0^b (Kron, Å) (5)	$\log L_{Ly\alpha}^a$ ($2''$, erg s $^{-1}$) (6)	$\log L_{Ly\alpha}^b$ (Kron, erg s $^{-1}$) (7)	Local density ^c (arcmin $^{-2}$) (8)	z_{spec} (9)	Note (10)	Ref (11)
87	258.42478	50.44801	72.6	49	42.325	42.433	0.371
88	258.28013	50.43421	71.7	70.6	42.195	42.209	0.285
89	258.74664	50.30547	71.6	95.8	41.967	42.018	0.602
90	258.48008	50.37427	70.1	94.7	42.032	42.158	0.356
91	258.87704	50.31148	68.8	9.19	42.018	41.796	0.478
92	258.63292	50.37851	68.1	22.9	42.157	42.012	0.573
93	258.79403	50.28602	67.5	182	41.901	42.022	0.566
94	258.76861	50.45149	66.7	78.3	41.974	42.103	0.177
95	258.47060	50.43591	66.4	79.2	41.906	42.029	0.477
96	258.74194	50.12380	66.3	78	41.937	42.253	0.159
97	258.38649	50.09153	65.3	83.2	42.152	42.281	0.24
98	258.50209	50.21177	65	73.9	42.018	42.113	0.287
99	258.60530	50.31925	64.3	49.3	41.903	41.955	0.752
100	258.44428	50.33453	62.9	63	41.933	41.95	0.248
101	258.44827	50.24072	62.7	79	42.059	42.232	0.496
102	258.66369	50.31116	62.1	70.5	42.117	42.161	0.507
103	258.85948	50.06382	62.1	38.2	42.008	42.126	0.18
104	258.79800	50.24555	61.6	66.1	41.908	41.874	0.489
105	258.89831	50.33377	61.3	56.5	42.102	42.269	0.328
106	258.83134	50.36156	60.6	76.8	42.211	42.321	0.431
107	258.88995	50.26075	60.1	32.6	42.022	42.048	0.343
108	258.45175	50.24364	59.9	37.2	42.311	42.5	0.493
109	258.59660	50.24556	59.3	48.5	42.13	42.283	0.431
110	258.83743	50.35944	57.4	65	42.308	42.385	0.406
111	258.90913	50.10798	56.7	48.9	41.945	41.995	0.291
112	258.80991	50.35190	56.2	63.1	42.488	42.593	0.548
113	258.58895	50.40452	56.1	57.5	41.857	41.844	0.484
114	258.92575	50.26044	55.6	59.8	41.981	42.083	0.281
115	258.83696	50.22602	55.4	48.2	41.896	41.932	0.429
116	258.81953	50.28111	53.6	94.3	42.334	42.577	0.448
117	258.49476	50.20933	53.3	67.8	42.134	42.317	0.312
118	258.31804	50.44735	52.9	43.2	42.015	41.991	0.302
119	258.31281	50.39478	52.7	52.8	41.854	41.845	0.172
120	258.27443	50.08565	52.7	32.6	42.01	41.992	0.19
121	258.80919	50.09795	52.5	44.7	42.714	42.783	0.34
122	258.81510	50.20662	52.3	75	41.994	42.156	0.472
123	258.49573	50.41455	52.2	49.5	41.922	41.912	0.557
124	258.26555	50.35800	50.8	44.3	41.965	42.016	0.146
125	258.77224	50.29308	50.7	51.1	42.254	42.352	0.644
126	258.46599	50.16240	50.5	58.6	42.616	42.754	0.361
127	258.23890	50.14443	49.8	74.1	41.984	42.149	0.175
128	258.68647	50.29608	49.3	51.1	43.663	43.725	0.452	2.393	QSO	5
129	258.62099	50.26584	48.9	11.2	41.914	41.691	0.432

TABLE 1—*Continued*

53W002F- LAE# (1)	R.A. (deg) (2)	Dec. (deg) (3)	EW_0^a ($2''$, Å) (4)	EW_0^b (Kron, Å) (5)	$\log L_{Ly\alpha}^a$ ($2''$, erg s $^{-1}$) (6)	$\log L_{Ly\alpha}^b$ (Kron, erg s $^{-1}$) (7)	Local density ^c (arcmin $^{-2}$) (8)	z_{spec} (9)	Note (10)	Ref (11)
130	258.51501	50.27515	48.4	28.9	42.25	42.259	0.679
131	258.66634	50.38061	48.4	53.3	42.707	42.793	0.726
132	258.76418	50.28445	48	49.2	43.536	43.591	0.632
133	258.86771	50.17787	48	48.7	42.359	42.593	0.384
134	258.90682	50.11938	47.8	50.6	42.358	42.395	0.297
135	258.76462	50.23466	47.6	46.1	42.557	42.768	0.408
136	258.55367	50.32163	47.6	59.8	41.952	42.237	0.709
137	258.57258	50.44182	47.4	77.9	42.011	42.442	0.342
138	258.74577	50.41784	46.9	15.6	42.313	42.291	0.451
139	258.39931	50.08618	46.7	49.2	41.859	41.88	0.239
140	258.63872	50.20249	46.5	34.5	42.062	42.062	0.227
141	258.91421	50.22424	46.3	40.3	41.849	41.911	0.3
142	258.24874	50.10857	46.1	61	42.077	42.221	0.294
143	258.82584	50.12873	45.9	24.3	41.908	41.863	0.487
144	258.18393	50.10280	44.9	105	41.956	42.229	0.196
145	258.56131	50.25854	44.5	55.4	43.02	43.398	0.567	2.390	LAB/radio(53W002)	1
146	258.62468	50.24577	44.3	55.8	41.97	42.081	0.388
147	258.82171	50.19107	44.2	68	41.867	42.08	0.443
148	258.69763	50.26738	44.2	45	41.857	41.924	0.376
149	258.68439	50.38154	44	65.6	41.979	42.304	0.772
150	258.67207	50.37350	43.8	33.4	42.751	42.791	0.739
151	258.75152	50.40039	43.3	47	41.943	41.947	0.611
152	258.59872	50.32251	43.2	27.9	42.274	42.459	0.747
153	258.51080	50.29783	42	30	41.99	42.09	0.675
154	258.19402	50.30009	41.2	33.3	41.864	41.868	0.187
155	258.83558	50.39516	41	42.1	41.869	41.94	0.319
156	258.43681	50.40042	41	23.7	41.823	41.747	0.395
157	258.91729	50.30043	40.8	53.6	42.067	42.14	0.338
158	258.26870	50.33844	40.4	50.4	42.656	42.792	0.16
159	258.78601	50.40570	39.1	38.5	41.824	41.857	0.455
160	258.74111	50.36884	38.7	37.5	41.804	41.862	0.749
161	258.25919	50.46269	38.7	42.2	41.945	42.041	0.228
162	258.45812	50.18303	38.1	48.8	41.862	42.012	0.389
163	258.77423	50.43241	37.8	26.3	41.867	41.945	0.329
164	258.51679	50.29996	37.7	25.4	41.939	41.949	0.736
165	258.69815	50.36658	36.9	61	41.817	42.125	0.732
166	258.65537	50.24716	36.2	40.1	42.333	42.523	0.345
167	258.39421	50.06690	36.1	42.2	41.894	42.003	0.192
168	258.54232	50.14515	35.6	29.3	42.206	42.29	0.208
169	258.45903	50.44120	35.6	34.3	43.004	43.044	0.454
170	258.83864	50.15230	35.4	32.3	41.863	41.915	0.484
171	258.49989	50.38673	35.3	46.5	42.039	42.214	0.466
172	258.68790	50.41428	35	56.2	41.888	42.208	0.487

TABLE 1—*Continued*

53W002F- LAE# (1)	R.A. (deg) (2)	Dec. (deg) (3)	EW_0^a ($2''$, Å) (4)	EW_0^b (Kron, Å) (5)	$\log L_{Ly\alpha}^a$ ($2''$, erg s $^{-1}$) (6)	$\log L_{Ly\alpha}^b$ (Kron, erg s $^{-1}$) (7)	Local density ^c (arcmin $^{-2}$) (8)	z_{spec} (9)	Note (10)	Ref (11)
173	258.41522	50.22304	33.7	44.5	42.53	42.838	0.384
174	258.67622	50.38493	33.5	112	42.17	42.557	0.746
175	258.77025	50.25271	33.1	26.1	42.001	41.958	0.489
176	258.66970	50.14040	33.1	21.9	41.872	41.899	0.144
177	258.80325	50.39305	32.4	31.2	41.974	42.03	0.476
178	258.47835	50.18144	31.1	76.2	41.934	42.206	0.36
179	258.61658	50.31336	31	34.5	41.824	41.899	0.721
180	258.88997	50.30360	30.9	42.7	42.411	42.678	0.43
181	258.69585	50.39219	30.5	45.9	41.977	42.209	0.754
182	258.76024	50.30220	30	24.5	41.827	41.835	0.641
183	258.62920	50.33774	29.4	26.5	41.812	41.902	0.666
184	258.74899	50.36302	29.4	22.8	41.851	41.873	0.719
185	258.44206	50.15688	29.2	1.4	41.906	41.009	0.33
186	258.95391	50.34714	28.6	22.5	41.914	41.919	0.133
187	258.89764	50.19231	28.4	29.7	42.006	42.068	0.295
188	258.61821	50.30841	28.3	45.9	42.246	42.485	0.663
189	258.39907	50.31853	28	48	42.249	42.61	0.186
190	258.72235	50.30051	28	39.1	42.128	42.314	0.564
191	258.80768	50.13504	28	39.3	42.662	42.878	0.443
192	258.50710	50.43131	27.8	29.2	42.043	42.159	0.478
193	258.61556	50.33513	27.5	20.7	42.343	42.457	0.701
194	258.54895	50.38175	27.4	20.6	41.803	41.872	0.48
195	258.52324	50.31402	26.5	23.5	41.848	41.92	0.677
196	258.91109	50.31318	26.3	38.1	42.101	42.343	0.383
197	258.78178	50.32572	26.2	14.8	41.96	42.011	0.562
198	258.84587	50.32118	26.1	-3.5	41.958	NAN	0.489
199	258.58729	50.41828	26	25.3	41.979	42.106	0.437
200	258.86927	50.24480	25.9	25.5	42.17	42.202	0.355
201	258.54722	50.26959	25.9	34.4	43.418	43.589	0.694	2.397	LAB/QSO(No.19)	2,3,5
202	258.83695	50.32071	25.6	14.8	41.939	42.023	0.501
203	258.83118	50.13003	25.5	23	41.809	41.803	0.487
204	258.79140	50.19397	25.4	39.7	41.885	42.071	0.393

^aThe fourth and sixth rows are based on the fixed aperture ($2''$) photometry.

^bThe fifth and seventh rows are based on the Kron photometry.

^cThe local densities are estimated by smoothing the LAE number density with Gaussian kernel with $\sigma=1'.5$.

References. — (1) Windhorst et al. 1991; (2) Pascarelle et al. 1996a; (3) Pascarelle et al. 1996b; (4) Pascarelle et al. 1998; (5) Keel et al. 1999; (6) Smail et al. 2003.

NOTE.—There are a few artificial values in this table. The EW_0 (Kron) of 53W002F-LAE2 and LAE11 are replaced by “ ∞ ” because our EW_0 calculation

gives the continuum fluxes of negative values for these objects. For LAE198, the $\log L_{Ly\alpha}$ (Kron) is described as “NAN” since we obtained the negative $L_{Ly\alpha}$ (Kron).

A. THE CALCULATION OF THE EW FOR Ly α EMISSION LINES AT $z = 2.4$

Here we show the calculation method of the *EW* for Ly α at $z=2.4$ from the *NB413* and *B*-band fluxes.

As the wavelength range of the *NB413* filter is overlapped with that of the *B*-band (see Figure 1) the continuum flux and the emission flux mix in the *NB413* flux and the *B* flux, respectively. The *NB413* flux and the *B* flux can be described as follows,

$$f_{\nu NB413} = f_{\nu C} + f_{\nu Ly\alpha}, \quad (\text{A1a})$$

$$f_{\nu B} = f_{\nu C} + f_{\nu Ly\alpha} \times \frac{\Delta\nu_{NB413}}{\Delta\nu_B}. \quad (\text{A1b})$$

$f_{\nu NB413}/f_{\nu B}$ is the flux per unit frequency ($\text{erg s}^{-1} \text{cm}^{-2} \text{Hz}^{-1}$) for the photons that enter the *NB413*/*B*-band filter, respectively. On the other hand, $f_{\nu Ly\alpha}/f_{\nu C}$ is the flux per unit frequency of the Ly α line component/the continuum component at the wavelength of 4140 Å, respectively. $\Delta\nu_{NB413}$ and $\Delta\nu_B$ is the width of the *NB413* and *B* band filters (*FWHM*) in unit of frequency, respectively. Here we assume the flat spectrum of the continuum ($f_{\nu C} = \text{constant}$) in the range of the *B* band because we cannot estimate the continuum slope at $\lambda = 4140$ Å from only the *B* and *NB413* fluxes.

From (A1a) and (A1b),

$$f_{\nu Ly\alpha} = \frac{\Delta\nu_B}{\Delta\nu_B - \Delta\nu_{NB413}} (f_{\nu NB413} - f_{\nu B}), \quad (\text{A2a})$$

$$f_{\nu C} = \left(1 - \frac{\Delta\nu_B}{\Delta\nu_B - \Delta\nu_{NB413}}\right) f_{\nu NB413} + \frac{\Delta\nu_B}{\Delta\nu_B - \Delta\nu_{NB413}} f_{\nu B}. \quad (\text{A2b})$$

These fluxes per unit frequency lead the several physical quantities of the Ly α emission and the continuum. For the Ly α emission, the flux ($\text{erg s}^{-1} \text{cm}^{-2}$) is

$$F_{Ly\alpha} = f_{\nu\alpha} \times \Delta\nu_{NB413} = \frac{\Delta\nu_B \Delta\nu_{NB413}}{\Delta\nu_B - \Delta\nu_{NB413}} (f_{\nu NB413} - f_{\nu B}), \quad (\text{A3})$$

and the luminosity (erg s^{-1}) is

$$L_{Ly\alpha} = 4\pi d_L^2 F_{Ly\alpha}, \quad (\text{A4})$$

where d_L is the luminosity distance at $z = 2.4$; 19,830 Mpc in the cosmology we adopted.

For the continuum, the flux per unit wavelength is

$$f_{\lambda C} = \frac{c}{\lambda^2} f_{\nu C}, \quad (\text{A5})$$

where $\lambda = 4140$ Å.

Using (A2b), (A3), and (A5), the *EW* in rest frame can be calculated as

$$EW_0 = \frac{F_{Ly\alpha}}{f_{\lambda C}} \times \frac{1}{(1+z)}. \quad (\text{A6})$$

B. THE MAKING OF THE Ly α IMAGE AND THE CONTINUUM IMAGE

In order to make the Ly α image and the continuum image, we should subtract the continuum component from *NB413* image or the Ly α line component from the *B* image. It is possible to do so using the *NB413* image and the *B* image, but careful treatment is needed because the quality of the final image is sensitive to the number of the image operation.

The relation between the magnitude and the count in the each image is

$$m_{NB413} = -2.5 \log(COUNT_{NB413}) + Z_{NB413}, \quad (\text{B1a})$$

$$m_B = -2.5 \log(COUNT_B) + Z_B, \quad (\text{B1b})$$

where Z is the zero point magnitude of each image; 31.73 for the $NB413$ image and 33.85 for the B image. From these the fluxes per unit frequency can be described as follows,

$$f_{\nu NB413} = COUNT_{NB413} \times 10^{-0.4(Z_{NB413}+48.6)}, \quad (B2a)$$

$$f_{\nu B} = COUNT_B \times 10^{-0.4(Z_B+48.6)}. \quad (B2b)$$

From (A2a) the $Ly\alpha$ flux per unit frequency is described as

$$f_{\nu Ly\alpha} = \frac{\Delta\nu_B}{\Delta\nu_B - \Delta\nu_{NB413}} \times 10^{-0.4(Z_B+48.6)} \{10^{0.4(Z_B-Z_{NB413})} COUNT_{NB413} - COUNT_B\}, \quad (B3)$$

and the equation of the $Ly\alpha$ magnitude is

$$\begin{aligned} m_{Ly\alpha} &= -2.5 \log(f_{\nu Ly\alpha}) - 48.6 \\ &= -2.5 \log\{10^{0.4(Z_B-Z_{NB413})} COUNT_{NB413} - COUNT_B\} + Z_B + 2.5 \log\left(1 - \frac{\Delta\nu_{NB413}}{\Delta\nu_B}\right). \end{aligned} \quad (B4)$$

Therefore if we take the $Ly\alpha$ image and the zero point of the image as

$$\begin{aligned} Ly\alpha_image &= 10^{0.4(Z_B-Z_{NB413})} \times NB413_image - B_image \\ &= 7.047 \times NB413_image - B_image, \end{aligned} \quad (B5a)$$

$$Z_{Ly\alpha} = Z_B + 2.5 \log\left(1 - \frac{\Delta\nu_{NB413}}{\Delta\nu_B}\right), \quad (B5b)$$

(B4) becomes

$$m_{Ly\alpha} = -2.5 \log(COUNT_{Ly\alpha}) + Z_{Ly\alpha}. \quad (B6)$$

So we made the $Ly\alpha$ image as (B5a).

We made the continuum image in the same way. From (A2b), (B2a), and (B2b),

$$f_{\nu C} = \frac{\Delta\nu_{NB413}}{\Delta\nu_B - \Delta\nu_{NB413}} \times 10^{-0.4(Z_{NB413}+48.6)} \left\{ \frac{\Delta\nu_B}{\Delta\nu_{NB413}} 10^{0.4(Z_{NB413}-Z_B)} COUNT_B - COUNT_{NB413} \right\}, \quad (B7)$$

and

$$m_C = -2.5 \log\left\{ \frac{\Delta\nu_B}{\Delta\nu_{NB413}} 10^{0.4(Z_{NB413}-Z_B)} COUNT_B - COUNT_{NB413} \right\} + Z_{NB413} + 2.5 \log\left(\frac{\Delta\nu_B}{\Delta\nu_{NB413}} - 1\right). \quad (B8)$$

Therefore we made the continuum image and the zero point of the image as

$$\begin{aligned} continuum_image &= \frac{\Delta\nu_B}{\Delta\nu_{NB413}} 10^{0.4(Z_{NB413}-Z_B)} \times B_image - NB413_image \\ &= 1.683 \times B_image - NB413_image, \end{aligned} \quad (B9a)$$

$$Z_{continuum} = Z_{NB413} + 2.5 \log\left(\frac{\Delta\nu_B}{\Delta\nu_{NB413}} - 1\right). \quad (B9b)$$

REFERENCES

- Benson, A. J., Frenk, C. S., Baugh, C. M., Cole, S., & Lacey, C. G. 2001, *MNRAS*, 327, 1041
- Bertin, E., & Arnouts, S. 1996, *A&AS*, 117, 393
- Binggeli, B., Sandage, A., & Tammann, G. A. 1988, *ARA&A*, 26, 509
- Cassata, P. et al. 2011, *A&A*, 525, 143
- Coles, P., & Jones, B. 1991, *MNRAS*, 248, 1
- Croton, D. J. et al. 2005, *MNRAS*, 356, 1155
- Davis, M., & Peebles, P. J. E. 1977, *ApJS*, 34, 425
- Dressler, A. 1980, *ApJ*, 236, 351
- Goto, T., Yamauchi, C., Fujita, Y., Okamura, S., Sekiguchi, M., Smail, I., Bernardi, M., & Gomez, P. L. 2003, *MNRAS*, 346, 601
- Gronwall, C. et al. 2007, *ApJ*, 667, 79
- Guaita, L. et al. 2010, *ApJ*, 714, 255G
- Hammer, F. et al. 1997, *ApJ*, 481, 49
- Hayashino, T. et al. 2004, *AJ*, 128, 2073
- Im, M., Yamada, T., Tanaka, I., & Kajisawa, M. 2002, *ApJ*, 578, L19
- Kaiser, N. 1987, *MNRAS*, 227, 1
- Kayo, I., Taruya, A., & Suto, Y. 2001, *ApJ*, 561, 22
- Keel, W. C., Cohen, S. H., Windhorst, R. A., & Waddington, I. 1999, *AJ*, 118, 2547
- Keel, W. C., Wu, W., Waddington, I., Windhorst, R. A., & Pascarelle, S. M. 2002, *AJ*, 123, 3041
- Kofman, L., Bertshinger, E., Gelb, J. M., Nusser, A., & Dekel, A. 1994, *ApJ*, 420, 44
- Komatsu, E. et al. 2009, *ApJS*, 180, 330
- Komatsu, E. et al. 2011, *ApJS*, 192, 18
- Kovač, K., Somerville, R. S., Rhoads, J. E., Malhotra, S., & Wang, J. 2007, *ApJ*, 668, 15
- Kuiper, E. et al. 2011, *A&A*, 417, 1088
- Malhotra, S., & Rhoads, J. 2002, *ApJ*, 565, 71
- Marinoni, C. et al. 2005, *A&A*, 442, 801
- Marinoni, C. et al. 2008, *A&A*, 487, 7
- Matsuda, Y. et al. 2004, *AJ*, 128, 569
- Matsuda, Y. et al. 2005, *ApJ*, 634, L125
- Matsuda, Y., Yamada, T., Hayashino, T., Yamauchi, R., & Nakamura, Y. 2006, *ApJ*, 640, L123
- Matsuda, Y. et al. 2011, *MNRAS*, 410, L13
- Matsuda, Y. et al. 2012, arXiv:1204.4934
- Miyazaki, S. et al. 2002, *PASJ*, 54, 833
- Mori, M. & Umemura, M. 2008, in *ASP Conf. Ser.* 399, *Panoramic Views of Galaxy Formation and Evolution*, ed. T. Kodama, T. Yamada, & K. Aoki (San Francisco, CA: ASP), 288
- Motohara, K., Yamada, T., Iwamuro, F., & Maihara, T. 2001a, in *ASP Conf. Ser.* 245, *Astrophysical Ages and Timescales*, ed. T. von Hippel, C. Simpson, & N. Manset (San Francisco: ASP), 634
- Motohara, K., et al. 2001b, *PASJ*, 53, 459
- Nakajima, K., et al. 2012, *ApJ*, 745, 12
- Nilsson, K. K. et al. 2007, *A&A*, 471, 71
- Nilsson, K. K., Tapken, C., Möller, P., Freudling, W., Fynbo, J. P. U., Meisenheimer, K., Laursen, P., & Östlin, G. 2009, *A&A*, 498, 13
- Ono, Y. et al. 2010, *MNRAS*, 402, 1580
- Ouchi, M. et al. 2004, *ApJ*, 611, 660
- Ouchi, M. et al. 2005, *ApJ*, 620, L1
- Ouchi, M. et al. 2008, *ApJS*, 176, 301
- Park, C., Choi, Y.-Y., Vogeley, M. S., Gott, J. R. I., & Blanton, M. R. 2007, *ApJ*, 658, 898
- Pascarelle, S. M., Windhorst, R. A., Driver, S. P., Ostrander, E. J., & Keel, W. C. 1996a, *ApJ*, 456, L21
- Pascarelle, S. M., Windhorst, R. A., Keel, W. C., & Odewahn, S. C. 1996b, *Nature*, 383, 45

- Pascarelle, S. M., Windhorst, R. A., & Keel, W. C. 1998, *AJ*, 116, 2659
- Pentericci, L. et al. 2000a, *A&A*, 361, L25
- Prescott, M.K.M., Kashikawa, N., Dey, A., & Matsuda, Y. 2008, *ApJ*, 678, L77
- Schlegel, D.J., Finkbeiner, D. P., & Davis, M. 1998, *ApJ*, 500, 525
- Shimasaku, K., et al. 2003, *ApJ*, 586, L111
- Smail, I., Ivison, R. J., Gilbank, D. G., Dunlop, J. S., Keel, W. C., Motohara, K., & Stevens, J. A. 2003, *ApJ*, 583, 551
- Steidel, C. C., et al. 2000, *ApJ*, 532, 170
- Steidel, C. C., Bogosavljević, M., Shapley, A. E., Kollmeier, J. A., Reddy, N. A., Erb, D. K., & Pettini, M., 2011, *ApJ*, 736, 160
- Stiavelli, M., Scarlata, C., Panagia, N., Treu, T., Bertin, G., & Bertola, F. 2001, *ApJ*, 561, L37
- Sullivan, M., Treyer, M. A., Ellis, R. S., Bridges, T. J., Milliard, B., & Donas, J. 2000, *MNRAS*, 312, 442
- Taylor, A. N., & Watts, P. I. R. 2000, *MNRAS*, 314, 92
- Treu, T., Ellis, R. S., Kneib, J.-P., Dressler, A., Smail, I., Czoske, O., Oemler, A., & Natarajan, P. 2003, *ApJ*, 591, 53
- Treyer, M. A., Ellis, R. S., Milliard, B., Donas, J., & Bridges, T. J. 1998, *MNRAS*, 300, 303
- Uchimoto, Y. K. et al. 2012, arXiv:1203.0814
- van Dokkum, P. G. 2001, *PASP*, 113, 1420
- Venemans, B. P. et al. 2002, *ApJ*, 569, L11
- Venemans, B. P. et al. 2004, *A&A*, 424, L17
- Waddington, I. 1998, in *ASP Conf. Ser.* 146, *The Young Universe: Galaxy Formation and Evolution at Intermediate and High Redshift.*, ed. D'Odorico S., Fontana A., & Giallongo E. (San Francisco: ASP), 520
- Weinberg, D. H., Davé, R., Katz, N., & Hernquist, L. 2004, *ApJ*, 601, 1
- Windhorst, R. A. et al. 1991, *ApJ*, 380, 362
- Windhorst, R. A., Keel, W. C., & Pascarelle, S. M. 1998, *ApJ*, 494, L27
- Yagi, M., et al. 2002, *AJ*, 123, 66
- Yamada, T., et al. 2001, *PASJ*, 53, 1119
- Yamada, T. et al. 2012, *AJ*, 143, 79